Bifunctional ultrathin $RhRu_{0.5}$ alloy nanowire electrocatalysts for hydrazine assisted water splitting

Xiaoyang Fu, Dongfang Cheng, Chengzhang Wan, Simran Kumari, Hongtu Zhang, Ao Zhang, Huaixun Huyan, Jingxuan Zhou, Huaying Ren, Sibo Wang, Zipeng Zhao, Xun Zhao, Jun Chen, Xiaoqing Pan, Philippe Sautet, Yu Huang* and Xiangfeng Duan**

X. Fu, C. Wan, H. Zhang, H. Ren, S. Wang, Prof. P. Sautet and Prof. X. Duan
Department of Chemistry and Biochemistry
University of California
Los Angeles, CA 90095, USA
E-mail: sautet@ucla.edu
E-mail: xduan@chem.ucla.edu

D. Cheng, S. Kumari, Prof. P. Sautet
Department of Chemical and Biomolecular Engineering
University of California
Los Angeles, CA 90095, USA
E-mail: sautet@ucla.edu

X. Fu, C. Wan, A. Zhang, J. Zhou, Z. Zhao, and Prof. Y. Huang
Department of Materials Science and Engineering
University of California
Los Angeles, CA 90095, USA
E-mail: yhuang@seas.ucla.edu

H. Huyan, Prof. X. Pan
Department of Materials Science and Engineering
University of California
Irvine, CA 92697, USA

X. Zhao, Prof. J. Chen
Department of Bioengineering
University of California
Los Angeles, CA 90095, USA

Keywords: hydrazine oxidation reaction, electrocatalysis, nanomaterials, noble metal, hydrazine assisted water splitting

Abstract

Hydrazine assisted water electrolysis offers a feasible path for low-voltage green hydrogen production. Herein we report the design and synthesis of ultrathin $RhRu_{0.5}$ alloy wavy nanowires as bifunctional electrocatalysts for both anodic hydrazine oxidation reaction (HzOR) and cathodic hydrogen evolution reaction (HER). We show that the $RhRu_{0.5}$ alloy wavy nanowires can achieve total electrooxidation of hydrazine with lower overpotential and high mass activity as well as improved performance for HER, which together, leads to ultrahigh performance for hydrazine assisted water electrolysis, with ultralow cell voltage of 54 mV at current density of 100 mA/cm^2 and ultrahigh current density of 853 mA/cm^2 at a cell voltage of 0.6 V. The resulting electrocatalysts further demonstrate a stable operation at a high current density of 100 mA/cm^2 for 80 hours of testing period with little degradation. The overall performance not only far exceeds the performances of the previously reported hydrazine assisted water electrolyzers, but also equivalent to a high turnover frequency (TOF) value of 1618/h for catalytic hydrazine decomposition at room temperature, which outperforms many previously reported catalysts (TOF < 500/h at room temperature).

1 Introduction

Hydrazine assisted water electrolysis can greatly lower the required voltage and energy consumption for green hydrogen production by replacing the sluggish oxygen evolution reaction (OER) in conventional water electrolysis with HzOR. Hydrazine is widely employed in chemical and pharmaceutical industry[1], and the waste water containing hydrazine is carcinogenic and toxic[2-3]. Therefore, hydrazine assisted water electrolyzers can allow to convert hydrazine into hydrogen and nitrogen, thus offering a potential pathway for hazard removal while at the same time achieving green hydrogen production. Although catalytic hydrazine decomposition has also been studied[4-5], the hydrazine assisted water electrolyzer

offers the advantage of producing hydrogen in the cathode compartment without the need for nitrogen separation, and thus has attracted considerable recent interests[6].

Since the cathodic HER is essentially the same as that of the common water electrolysis, the anodic HzOR represents the key reaction for hydrazine assisted water splitting. In particular, a total electrooxidation is essential, not only for the efficient utilization of hydrazine, but also for preventing the potential generation of harmful byproducts (*e.g.,* NH_3) rather than the environmentally friendly N_2. Although many electrocatalysts based on less costly metals (*e.g.* Ni[7], Co[8-9], Ru[10-11], etc.) have been explored for HzOR to date, they are generally unable to achieve the total electrooxidation of hydrazine[12] and produce NH_3 as an undesired byproduct[13] from differential electrochemical mass spectrometry (DEMS) and rotation disk electrode (RDE) study, which is consistent with theoretical studies that suggests some non-noble metal (*e.g.* Ni) could facilitate both N-H cleavage and N-N cleavage and lead to incomplete hydrazine oxidation[14].

On the other hand, noble metals (*e.g.,* Rh, Pt and Pd) have been shown capable of facilitating the total oxidation of hydrazine with a charge transfer number of four[12]. Among them, Rh exhibits the lowest half wave potential for HzOR[12], and therefore represents a primary choice of electrocatalyst. Considering the scarcity and high cost of the noble metal based electrocatalysts, it is essential to develop highly effective electrocatalyst with high mass activity (MA) to lower the required mass loading. Ru typically exhibits lower onset and half wave potential for HzOR but cannot achieve the total electrooxidation based on the previous RDE studies[14]. Thus, alloying Ru with Rh based electrocatalysts may bring synergistic benefits to lower the overpotential while simultaneously achieving total oxidation of hydrazine[12]. RhRu-based alloy has also been explored as electrocatalysts for the HER[15-16], OER[17-18] and nitrogen reduction reaction (NRR)[19]. Nonetheless, its potential application for HzOR has not been explored before.

The HER on the cathode side is also important for the electrolysis and RhRu alloy has also been visited as a good electrocatalyst[15-16], with the proposed mechanism that Ru site favors the dissociative adsorption of -OH to facilitate the -H adsorption on Rh sites, while at the same time weakens the binding with H_{ad} to boost HER performance.

ECSA is also an essential factor in determining the mass activity. Ultrathin wavy nanowires have been shown to exhibit high ECSA, which typically feature high specific surface area because of the ultrathin diameter[20-21], rich surficial defects and potentially catalytic sites thanks to the wavy surface and good charge transport due to the one-dimensional nanostructure[20, 22-23].

Herein we report the design and synthesis of ultrathin $RhRu_{0.5}$ alloy wavy nanowires as a bifunctional electrocatalyst for both HzOR and HER. The introduction of Ru considerably lowers the overpotential of the HzOR and thus greatly enhances the performances with an ultrahigh MA of 60.4±6.2 A/mg at 0.20 V vs. RHE from the tests on carbon paper, which nearly doubles than that of the Rh wavy nanowires (37.6±2.1 A/mg at 0.20 V vs. RHE) and is over one order of magnitude higher than that of the commercial Pt on graphitized carbon (Pt/GC). RDE tests reveals an electron transfer number of four, proving the total oxidation of hydrazine to environmentally friendly nitrogen gas. In addition, the $RhRu_{0.5}$ alloy wavy nanowires also exhibit better HER performance than Rh wavy nanowires and commercial Pt/GC electrocatalysts. Together, by using the $RhRu_{0.5}$ alloy wavy nanowires as both the HzOR and HER catalysts, the hydrazine assisted water electrolyzer delivers a current density 100 mA/cm^2 at very low overpotentials of 54 mV and a high current density of 853 mA/cm^2 at 0.6 V. Chronopotentiometry (CP) tests also demonstrated robust long-term stability over the 80-hour testing period.

2 Results and discussion

2.1 Characterization

The TEM images reveal the resulting $RhRu_{0.5}$ and Rh ultrafine wavy nanowire morphologies with an average diameter: 2.6±0.5 nm and highly jagged surface (**Figure 1A, 1B and Figure S1A**). The high resolution TEM image (HRTEM) reveals a lattice spacing of 0.22 nm, consistent with (111) facet (**Figure 1C**). In contrast, the monometallic Ru synthesized under this condition exhibits a nanoparticle morphology (**Figure S1B**). The ultrathin diameter with highly jagged surface could contribute to increased surface active sites and lead to ultrahigh ECSA, and the one-dimensional morphology can benefit the charge transport to and from the surface active sites, which is essential for efficient electrocatalysis.

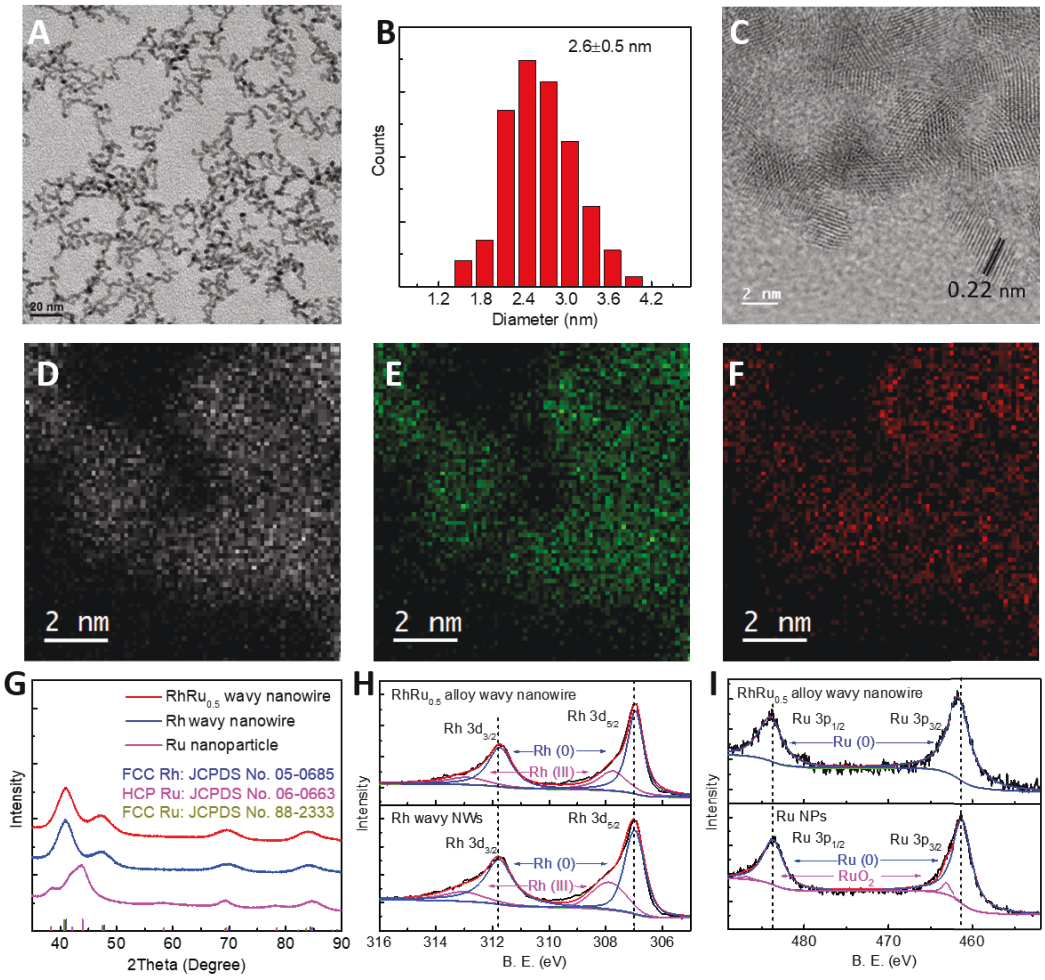

Figure 1. (A) TEM pictures of $RhRu_{0.5}$ wavy nanowires. (B) Diameter distribution of $RhRu_{0.5}$ wavy nanowires. (C) High resolution TEM picture of $RhRu_{0.5}$ wavy nanowires. (D) STEM of $RhRu_{0.5}$ wavy nanowires and EDX mapping of Rh (E) and Ru (F) elements. (G) XRD of $RhRu_{0.5}$ alloy wavy nanowires, Rh wavy nanowires and Ru nanoparticles. (H) XPS spectra of Rh for $RhRu_{0.5}$ alloy wavy nanowires and Rh wavy nanowires. (I) XPS spectra of Ru for $RhRu_{0.5}$ alloy wavy nanowires and Ru nanoparticles.

The STEM image (**Figure 1D**) and the corresponding EDX mapping images for Rh and Ru (**Figure 1E and 1F**) demonstrates uniform distribution of Rh and Ru elements in the nanowire structures. A quantification of EDX signal gives an Rh:Ru atomic ratio of 66.5%:33.5% (**Figure S2**), which agrees well with the ICP-AES (Ru:Rh=0.529±0.033:1) results. The XRD study (**Figure 1G**) demonstrates very similar pattern for the $RhRu_{0.5}$ wavy nanowires compared with Rh wavy nanowires with face centered cubic (FCC) (JCPDS No. 05-0685) crystal structure with peaks corresponding to the characteristic (111), (200), (220) and (311) crystal planes. While the Ru nanoparticle synthesized under the same condition demonstrates hexagonal close-packed (HCP) (JCPDS No. 06-0663) crystal structure, indicating the formation of the alloy phase in $RhRu_{0.5}$ wavy nanowires promotes the growth of Ru into the FCC lattice. Similar phenomenon has also been reported in the previous literatures regarding RhRu alloys as well[15]. XPS studies reveal the binding energy of Rh in $RhRu_{0.5}$ alloy wavy nanowires is slightly downshifted by ~0.05 eV from that of Rh wavy nanowires (**Figure 1H**); while the binding energy of Ru is upshifted by 0.30 eV from that of monometallic Ru nanoparticles (**Figure 1I**), indicating the slight charge transfer from Ru to Rh. Such a charge transfer is consistent with the electronegativity difference between Rh (2.20) and Rh (2.28). XPS analysis also reveals a surficial atomic ratio of Rh:Ru is 2.19:1.00, which is also similar to the ICP-AES and EDS results. AFM studies also confirm a nanowire network morphology (**Figure S3A**) with the line profile showing the nanowire thickness of ~2 nm (**Figure S3B**), consistent with the TEM studies

2.2 Electrochemical study

The electrochemical performance of the nanowire catalysts was first studied via CV to determine the $ECSA_{HUPD}$ (**Figure 2**A). Significantly, the $RhRu_{0.5}$ wavy nanowires exhibit an ultrahigh ECSA of 101.3±3.1 m^2/g, thanks to the ultrathin diameter and highly jagged

electrochemically accessible surface. Similarly, the Rh wavy nanowires also demonstrate a high ECSA of 101.0±1.3 m^2/g .

The CV studies show that the peaks for hydrogen adsorption and desorption of the $RhRu_{0.5}$ nanowires shift to lower potential in comparison with Rh nanowires, indicating weakened hydrogen desorption upon the introduction of Ru, which can potentially benefit HER and similar phenomenon has also been reported for the PtRu based nanomaterials [24].

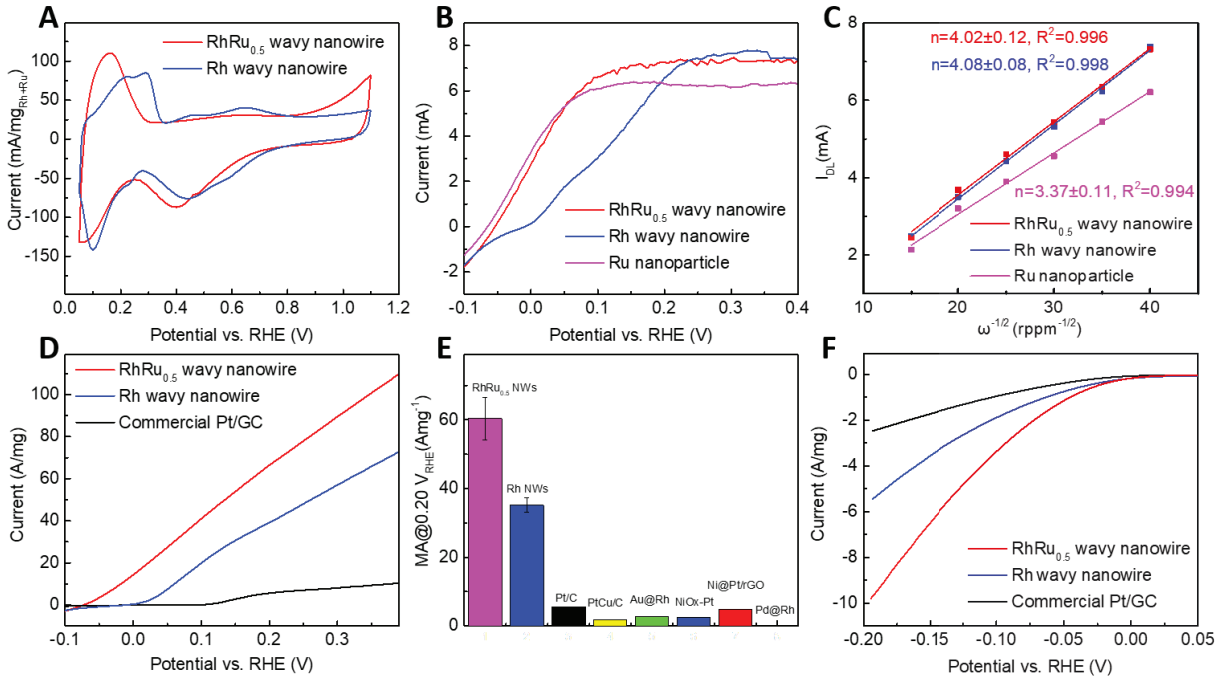

Figure 2. Electrochemical study. (A) CV curves of the $RhRu_{0.5}$ alloy wavy nanowire and Rh wavy nanowire in 1.0 M KOH electrolyte for ECSA determination. (B) LSV curves of $RhRu_{0.5}$ alloy wavy nanowire, Rh wavy nanowire and Ru nanoparticle in 1.0 M KOH + 10 mM N_2H_4 electrolyte at rotation rate of 1600 rppm. (C) Linear fitting of the diffusion limited current at different rotation rate. (D) LSV curves of $RhRu_{0.5}$ alloy wavy nanowire, Rh wavy nanowire and Ru nanoparticle in 1.0 M KOH + 0.10 M N_2H_4 electrolyte tested on carbon paper electrode. (E) Comparison of the MA at 0.20 V vs. RHE with the previously reported HzOR electrocatalysts. (F) LSV curves of the alloy wavy nanowire, Rh wavy nanowire and Ru nanoparticle in 1.0 M KOH electrolyte at rotation rate of 1600 rppm.

The preliminary HzOR catalytic activity was conducted in the electrolyte of 1.0 M KOH and 0.010 M hydrazine. The LSV demonstrates a current plateau (**Figure 2B)**, indicating a diffusion limited current ~7.4 mA for the $RhRu_{0.5}$ alloy wavy nanowires, which is similar to that of the Rh wavy nanowires. The current plateau shows notable fluctuations, which is

attributed to the generation of N_2 gas during the reaction. Importantly, the $RhRu_{0.5}$ alloy wavy nanowires demonstrate improved performances for HzOR with much lower halfwave potential of 19 mV and open circuit potential of -51 mV compared with the Rh wavy nanowires (halfwave potential of 119 mV and open circuit potential of -6 mV).

It is important to evaluate the electron transfer number to determine complete or incomplete oxidation. To this end, we have conducted RDE studies at different rotation rate. The linear fitting between the diffusion limited current at different rotation speed and the square root of the corresponding rotation rate according to the Levich equation was carried out as shown below[12]:

$$I_{DL} = 0.201nFAD_R^{2/3}v^{-1/6}C\omega^{1/2}$$

The values of the coefficients from the previous literatures[12]: v=1.07×10^{-2} cm^2/s, F=96500 C/mol, A=0.196 cm^2, D_R=1.40×10^{-5} cm^2/s and C=0.010 mol/L. The linear fitting demonstrates good linear correlation (R^2>0.99) and yields an electron transfer number of 4.02±0.12 for $RhRu_{0.5}$ wavy nanowire, 4.08±0.08 for Rh wavy nanowire, confirming a total electrooxidation of hydrazine on Rh based electrocatalysts[12]. In contrast, the Ru nanoparticles are unable to achieve the total electrooxidation of hydrazine with a lower electron transfer number of 3.37±0.11, (**Figure 2C** and **Figure S4**), consistent with the previous literature[12], which negates the advantage of low halfwave potential and open circuit potential.

We next carried out electrochemical tests on the carbon paper electrode to explore the practical performance of our catalysts. Carbon paper electrodes are attractive since the porous nanostructures can greatly facilitate the nitrogen gas removal during the hydrazine electrooxidation process. Importantly, the $RhRu_{0.5}$ alloy wavy nanowire catalysts on carbon paper electrode delivers a high mass activity of 60.4±6.2 A/mg at 0.20 V vs. RHE for, nearly

double that of Rh nanowires (37.6±2.1 A/mg), and more than one order of magnitude higher than commercial Pt/GC (5.42±0.24 A/mg). In general, the $RhRu_{0.5}$ alloy wavy nanowires also demonstrate one order of magnitude higher mass activity than the previously reported noble metal based electrocatalysts, including PtCu/C[25], Au@Rh core-shell nanowire[26], NiO_x-Pt[27], Ni@Pt/RGO[28], Pd@Rh[29] electrocatalysts (**Figure 2E**). In addition, very high geometric current density (60.4±6.2 mA/cm^2 at 0.20 V vs. RHE) is also achieved for the $RhRu_{0.5}$ alloy wavy nanowires at 0.20 V vs. RHE, which is also comparable with the results from the previous literatures even at one order of magnitude lower noble metal loading on the electrode [25-29], which will be highly beneficial for practical device development. In addition, the CA tests were carried out (**Figure S5**) and the $RhRu_{0.5}$ alloy wavy nanowires can also maintain the optimized current density at 0.20 V vs. RHE after 1 h of test.

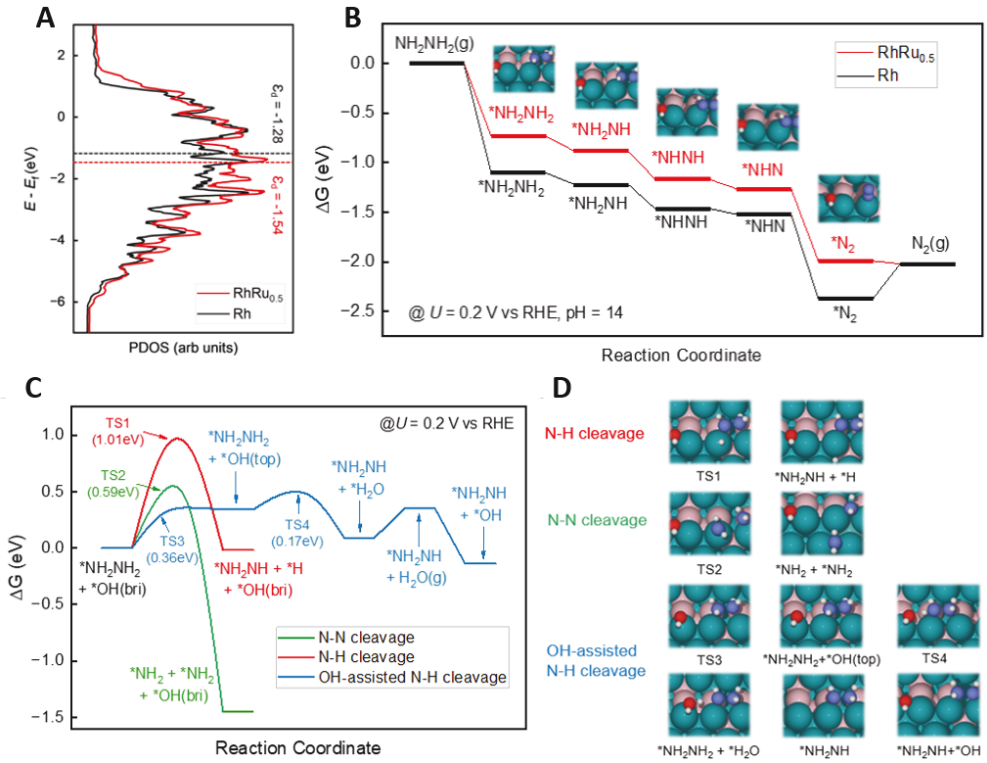

Figure. 3 (A) Electronic density of states projected on the surface Rh atom of $RhRu_{0.5}$ and Rh step sites. (B) The free energy of each step of HzOR on $RhRu_{0.5}$ and Rh step sites. (C) Calculated energy profile for each step of HzOR (including pathways leading to byproducts ammonia) at 0.2 V vs RHE. (D) Top view of the intermediates for the first step of HzOR on the hydroxylated RhRu0.5 step sites (labels refer to (C)).

We have further conducted theoretical studies to explore the role of Ru in facilitating HzOR. Our density functional theory (DFT) calculations of the projected densities of states (PDOS) reveal that the d-band center of the surface Rh atoms for the $RhRu_{0.5}$ alloy was downshifted from the Fermi level by 0.26 eV in comparison with Rh (**Figure 3A**), which weakens the interaction with adsorbates and facilitates the N_2 desorption step of HzOR (**Figure 3B**), leading to improved activity. In addition, although the N-N bond cleavage is thermodynamically favorable, N-H bond cleavage is more kinetically favorable with the assistance of adsorbed -OH group, with a lower energy barrier of 0.17 eV (and 0.36 eV for -OH migration) than that for N-N bond cleavage (0.59 eV) or that for the non OH-assisted N-H bond cleavage (**Figure 3C, D**). This underlines the key role of co-adsorbed -OH groups on the reaction selectivity.

The HER performance study was also carried out and the $RhRu_{0.5}$ alloy nanowires exhibit a mass activity of 1.89 A/mg at -0.07 V vs. RHE, which outperforms the Rh nanowires (1.11 A/mg at -0.07 V vs. RHE) and the commercial Pt/GC (0.57 A/mg at -0.07 V vs. RHE) (**Figure 2F**). In addition, lower Tafel slope was also observed (107.1 mV/dec) for $RhRu_{0.5}$ alloy nanowires, indicating more favorable kinetics (**Figure S6**). CP studies also demonstrate comparably better long-term performance than the Rh nanowires and commercial Pt/GC electrocatalysts during 10 hour of testing (**Figure S7**). The improved HER performance in $RhRu_{0.5}$ alloy can be attributed to the facilitated hydrogen desorption (**Figure 2A**). Additionally, our DFT studies indicate that, for the $RhRu_{0.5}$ alloy, the terrace hollow site (2Ru and 1Rh as shown in **Figure S8)** has an optimized ΔG_{H^*} value of -0.23 eV, which is more favorable than the counterpart in Rh electrocatalysts (**Figure S8**), indicating more facilitated hydrogen desorption and thus boosting HER performance upon the introduction of Ru.

2.4 Hydrazine assisted water electrolysis study

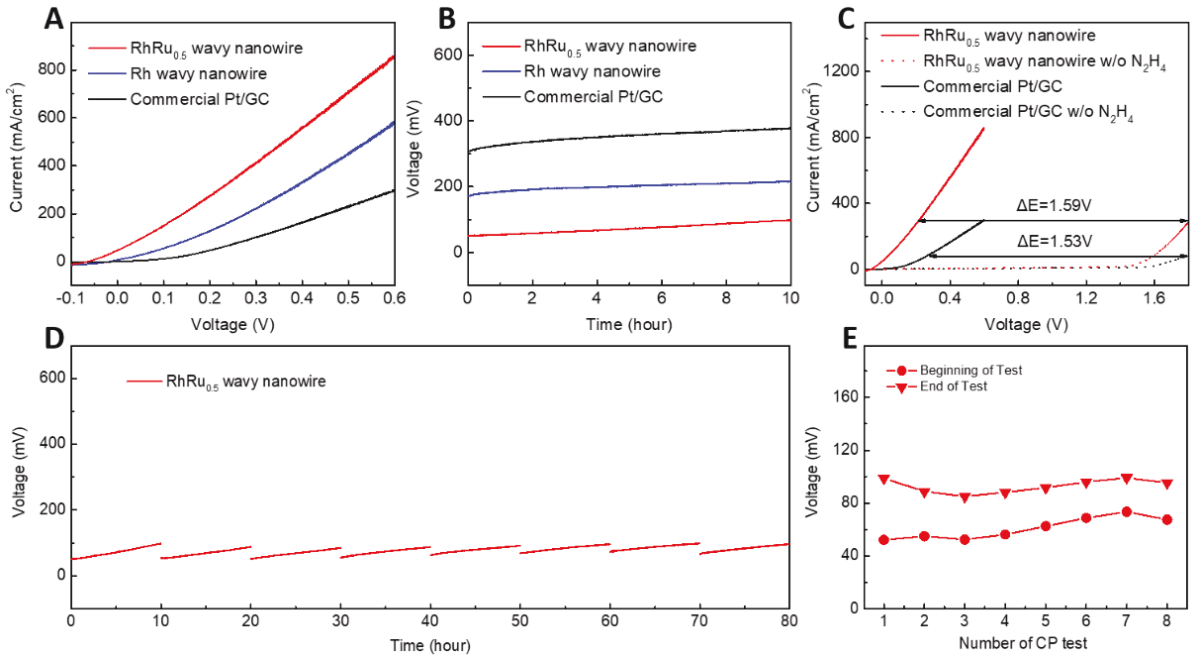

Figure 4. Hydrazine assisted water electrolyzer performances. (A) Polarization curves of the electrolyzer with $RhRu_{0.5}$ wavy nanowire||$RhRu_{0.5}$ wavy nanowire, Rh wavy nanowire||Rh wavy nanowire and commercial Pt/GC||commercial Pt/GC in the 1.0 M KOH+ 1.0 M N_2H_4 electrolyte at scan rate of 2 mV/s. (B) CP results of the electrolyzers at current density of 100 mA/cm^2. (C) Comparisons of the polarization curves of $RhRu_{0.5}$ wavy nanowire||$RhRu_{0.5}$ wavy nanowire and commercial Pt/GC||commercial Pt/GC in the 1.0 M KOH + 1.0 M N_2H_4 and 1.0 M KOH electrolyte, respectively. (D) Cumulative CP tests of the electrolyzer with $RhRu_{0.5}$ wavy nanowire||$RhRu_{0.5}$ wavy nanowire for 80 hours. (E) Cell voltage at the beginning and end of each 10-hour CP test.

Together, we have further assembled the full electrolyzer with $RhRu_{0.5}$ nanowires on carbon paper as both the anodic HzOR and cathodic HER electrocatalysts. Significantly, at a low mass loading of 0.20 mg/cm^2, the electrolyzer with $RhRu_{0.5}$ alloy wavy nanowire delivers a high current density of 100 mA/cm^2 at an ultralow voltages of 54 mV, and delivers an ultrahigh geometric current density of 853 mA/cm^2 at 0.6 V without any IR correction (Rs ~0.5 Ohm in **Figure S9**), which outperforms the electrolyzers employing Rh wavy nanowire (100 mA/cm^2 @165 mV, 586 mA/cm^2@0.6 V) and commercial Pt/C (100 mA/cm^2@296 mV, 298 mA/cm^2@0.6 V) (**Figure 4A**), and exhibits improved CP performance with much lower cell voltage (**Figure 4B**). EIS studies (**Figure S9**) reveal a smaller charge transfer resistance for $RhRu_{0.5}$ alloy nanowires (0.65 Ω) than that of Rh nanowire (1.38 Ω), which is consistent

with the improved activity observed for the electrolyzer with $RhRu_{0.5}$ alloy nanowire. The overall performance also notably outperforms all previously reported hydrazine assisted water electrolyzers (**Table 1**). In addition, with the assistance of hydrazine, electrolyzer can work at a much lower voltage than typical water electrolyzer without hydrazine. For example, 1.53 V was lowered in the Pt/GC||Pt/GC and 1.59 V was lowered in the $RhRu_{0.5}$ alloy wavy nanowire||$RhRu_{0.5}$ alloy wavy nanowire electrolyzer (**Figure 4C**).

The electrolyzer employing $RhRu_{0.5}$ alloy wavy nanowires also show excellent long-term performance with a stable lower cell voltage maintained for 10 h at current density 100 mA/cm^2. Importantly, although there is apparently an ~30-50 mV voltage increases after each 10 h test, the voltage increase can be partially attributed to the consumption of hydrazine during long-term electrolysis. Indeed, the performance can be largely recovered by refreshing the electrolyte with the original hydrazine concentration. Overall the electrolyzer can work at 100 mA/cm^2 for 80 hours with little performance decay (**Figure 3D**, **Figure S10**) with only 15.3 mV increase from the 1st to 8th 10-hour test (**Figure 3E**).

We have further characterized the electrocatalysts on anode and cathode after CP test. The TEM studies show that wavy nanowire morphology was generally retained after CP test (**Figure S11**). XRD reveal that the alloy phase remains after the CP test (**Figure S12**). EDS studies also confirm the elemental distribution and elemental ratio show little change after CP test (**Figure S13 and S14**). XPS study further confirm the binding energy and the elemental ratio remain similar (Rh:Ru=2.13:1.00 for cathode electrocatalysts and 2.18:1.00 for anode electrocatalysts, as shown in **Figure S15 and S16**). ICP-MS also confirmed that there is negligible electrocatalyst dissolution after CP test (<0.5% of the initial loading). These post reaction characterizations confirmed the robustness of our electrocatalysts. We also collected and measured the hydrogen gas produced from cathode compartment during the electrolysis via the water displacement method. The hydrogen measured experimentally is similar to the

theoretical value (**Figure S17**) and the Faradaic efficiency is calculated as 94.1%. In addition, we also carried out the characterization for the potential byproduct ammonia via spectrometry method. We cannot detect any ammonia production from the electrolysis process (**Figure S18**), indicating nitrogen gas as the only detectable product and confirming the total electrooxidation of hydrazine, consistent with 4-electron oxidation process determined from RDE studies.

In comparison with the conventional catalytic hydrazine decomposition for hydrogen production. Our system demonstrates a TOF value of 1009/h (calculated based on 100 mA current and detail is in the supplimentary info) at a negligible amount of electricity input (< 0.1 V). In addition, by lowering the electrocatalyst loading to 0.10 mg (**Figure S19**), we obtained the current of 80.2 mA at cell voltage of 54 mV, corresponding to a higher TOF value of 1618/h, which is much higher compared with the previously reported catalysts for hydrazine decomposition operating at room temperature (298-303 K) (**Table 2**).

Table 1. Comparison with the previous literature regarding hydrazine assisted water electrolyzer

Materials	Electrolyte	Electrolyzer performance	Reference
$RhRu_{0.5}$ alloy wavy nanowire	1.0 M KOH +1.0 M N_2H_4	-0.048 V @10.0 mA/cm^2 0.054 V@100 mA cm^2	This work
Rh wavy nanowire	1.0 M KOH +1.0 M N_2H_4	0.007 V @10.0 mA/cm^2 0.165 V@100 mA/cm^2	This work
Commercial Pt/GC	1.0 M KOH +1.0 M N_2H_4	0.088 V @10.0 mA/cm^2 0.296 V@100 mA/cm^2	This work
Rh/N-CBs	1.0 M KOH +0.5 M N_2H_4	0.2 V@20 mA/cm^2	[30]
Au@Rh core@shell nanowire	1.0 M KOH +0.1 M N_2H_4	0.18 V@10 mA/cm^2	[26]
Rh/RhOx nanosheet	1.0 M KOH +0.5 M N_2H_4	0.279 V@100 mA/cm^2 0.068 V @10 mA/cm^2	[31]
RuP_2/C	1.0 M KOH +0.3 M N_2H_4	0.023 V@10 mA/cm^2	[10]

Cu_1Ni_2-N	1.0 M KOH +0.5 M N_2H_4	0.24 V@10 mA/cm^2	[32]
Ni_2P	1.0 M KOH +0.5 M N_2H_4	0.45 V@100 mA/cm^2	[33]
NiCu alloy	1.0 M KOH +0.5 M N_2H_4	0.41 V@100 mA/cm^2	[34]
RhIr mesoporous nanoparticles	1.0 M KOH +0.5 M N_2H_4	0.13 V@10 mA/cm^2 0.604 V@100 mA/cm^2	[35]

Table 2. Comparison with the previous literature regarding the TOF of the catalysts for catalytic hydrazine decomposition reaction

Materials	Temperature	TOF	Reference
$RhRu_{0.5}$ alloy wavy nanowire	298K	1618/h	This work
Ni–Pt nanoparticles	298K	150/h	[36]
$Ni_{45}Rh_{55}/Ce(OH)CO_3$	303K	150/h	[37]
$Ni_{0.2}Rh_{0.8}$/rGO	323K	666.7/h	[38]
$Ni_{0.9}Pt_{0.1}/Ce_2O_3$	298K	28.1/h	[39]
$(Ni_3Pt_7)_{0.5}$–$(MnO_x)_{0.5}$/NPC-900	323K	706/h	[40]
$(Ni_3Pt_7)_{0.5}$–$(MnO_x)_{0.5}$/NPC-900	298K	120/h	[40]
Octahedral Ni–Pt/C	323K	210/h	[41]
Ni_3Pt_7/BNG-1000	298K	199.4/h	[42]
$CoPt_{0.034}/\gamma$-Al_2O_3	298K	117.8/h	[43]
$Ni_{0.8}Pt_{0.2}$/DT-$Ti_3C_2T_x$	323K	1220/h	[44]
Ni_5Pt_5-CeO_2	298K	416/h	[45]
Ni-Pt/MIL	323K	960/h	[46]
$Ni_{84}Pt_{16}$/graphene	298K	133/h	[47]
$Ni_{84}Pt_{16}$/graphene	323K	415/h	[47]
$Ni_{60}Pt_{40}/La_2O_3$	303K	448/h	[4]
Ni-Pt N-doped Carbon	323K	1602/h	[48]

3 Conclusion

In conclusion, we developed $RhRu_{0.5}$ alloy wavy nanowires via a facile solvothermal method. Thanks to the ultrahigh ECSA as well as the lowered d-band center in the $RhRu_{0.5}$ alloy, the resulting nanowire catalysts demonstrates exceptional performance for electrocatalytic HzOR with ultrahigh MA and low overpotential in addition to the capability to achieve the total electrooxidation of the hydrazine, greatly outperforming the previously reported noble metal based electrocatalysts. Good HER performances were also observed, which together leads to the hydrazine assisted water electrolyzer with unprecedented performance (54 mV@100 mA/cm^2, 853 mA/cm^2@0.6 V) as well as excellent long-term performances, which far exceeds all the previously reported hydrazine assisted water electrolyzers. Our study could open a pathway for efficiently converting the hazardous hydrazine into environmentally friendly products.

4 Methods

Chemicals

Sodium hexachlororhodate (III) (Na_3RhCl_6, analytical grade), Ruthenium chloride hydrate ($RuCl_3 \cdot xH_2O$, 38.0% - 42.0% Ru basis), sodium iodide (NaI, ACS reagent, ≥ 99.5%), polyvinylpyrrolidone (PVP, MW ~55,000), sodium ascorbate (NaAA, crystalline, ≥ 98%), hydrazine solution (35 wt% in water) and commercial Pt/GC (20%) were all purchased from Sigma-Aldrich. Carbon paper (Freudenberg H27) and anion exchange membrane (AEM) (FAS-50) were purchased from the fuelcell store. The electrolyzer device and the electric pump were purchased from Xi'an Yima Optoelec Co., Ltd.

Synthesis of $RhRu_{0.5}$ alloy wavy nanowires

The synthesis was carried out via a polyol method modified from the previous research[22-23]. 40 mg NaAA, 160 mg PVP and 75 mg NaI were mixed with 1.00 mL aqueous solution of Na_3RhCl_6 (10.0 mg/mL), 0.333 mL aqueous solution of $RuCl_3 \cdot xH_2O$ (10.0 mg/mL,

40-42% metal basis) and dissolved after ultra-sonication followed by adding 5.0 mL of ethylene glycol (EG). Then the vial was heated at 210 ^{o}C for 4 h and the post-synthetic treatment were carried out by washing/centrifuging with ethanol/acetone and ethanol/hexane. The final products were re-dispersed in ethanol. For comparison, the Rh wavy nanowire and Ru nanoparticles are synthesized at the same conditions with the addition of individual noble metal precursor only.

Structural characterizations

The transmission electron microscopy (TEM) was carried out on FEI T12 transmission electron microscope operated at 120 kV. The X-ray diffraction (XRD) was carried out on a Panalytical X'Pert Pro X-ray Powder Diffractometer with Cu-Kα radiation. X-ray photoelectron spectroscopy (XPS) was carried out with Kratos AXIS Ultra DLD spectrometer. The scanning transmission electron microscope (STEM) image and energy dispersive x-ray spectroscopy (EDX) mapping were carried out on Joel Jem-300CF (Grand Arm) operated at 300 kV. The inductively coupled plasma-atomic emission spectroscopy (ICP-AES) was carried out to determine the elemental ratio and loading of the electrocatalysts.

Electrochemical measurements

The electrochemical tests were carried out in a three-electrode cell system. The working electrode was an RDE with a geometric area of 0.196 cm^2 and the counter electrode was a Pt coil. The reference electrode was Hg/HgO (1.0 M KOH) and the potentials are converted against reversible hydrogen electrode (RHE) after calibration. The homogeneous ethanol dispersion of the electrocatalysts was dropcasted onto the RDE surface and dried under room temperature with Rh loading of 1.00 μg (5.1 μg/cm^2) for the $RhRu_{0.5}$ and Rh wavy nanowire, and Ru loading of 1.00 μg (5.1 μg/cm^2) for the Ru nanoparticle. Cyclic voltammetry (CV) was performed in Ar-saturated 1.0 M KOH electrolyte with a scan rate of 50 mV/s ranging from 0.05 to 1.10 V vs. RHE to determine the electrochemically active surface area ($ECSA_{HUPD}$).

HzOR tests were carried out in Ar-saturated electrolyte of 1.0 M KOH, 0.010 M hydrazine via linear sweep voltammetry (LSV) at a series of rotation rates of 225, 400, 625, 900, 1225 and 1600 rppm, with potential scan rate of 20 mV/s to study the electron transfer number. To probe the potential for real world applications, the HzOR tests were also carried out on the carbon paper electrode with the loading of 1.0 μg/cm^2 in the electrolyte of 1.0 M KOH, 0.10 M hydrazine via LSV. The chronoamperometry (CA) tests were carried out at 0.20 V vs. RHE for 1 h. The HER performances were tested on RDE with loading of 1.0 μg (5.1 μg/cm^2) via LSV in 1.0 M KOH electrolyte and the long-term performance was studied via CP at geometric current density of 10 mA/cm^2 for 10 h.

Hydrazine assisted water electrolysis test

Membrane electrode assembly process was employed with AEM sandwiched between two carbon paper electrodes with size of 1 cm^2 along with the PTFE gaskets and the electrocatalysts loading were 0.20 mg (Rh or Pt) for both anode and cathode. Electric pumps were employed to circulate the anolyte (1.0 M KOH + 1.0 M hydrazine) and catholyte (1.0 M KOH) at the flow rate of ~120 mL/min. LSV was carried out from -0.1 V to 0.6 V at 2 mV/s to obtain the polarization curves and CP at 100 mA/cm^2 was employed to probe the long-term performances of the electrolyzer. In order to detect the potential byproduct ammonia, 5% (w/v) Na_3PO_4 solution was used as buffer, 1.875 g phenol were dissolved in 3 ml methanol as phenol stock. Reagent A is prepared by mixing 3 ml phenol stock, 4mL 1.0 mg/mL sodium nitroprusside and 13 ml water. Reagent B is prepared by mixing 12 ml commercial bleach (3.5 % Cl) and 28 mL 27 % NaOH. 0.1 mL sample was taken out from the catholyte and anolyte, respectively, and mixed with 0.4 mL buffer, 1 mL Reagent A, 0.5 mL Reagent B and 3 mL water and then incubated under room temperature.

Computational

The vienna ab initio simulation package (VASP) was used to carry out all the periodic DFT calculations. The Perdew-Burke-Ernzerhof (PBE) parametrization of the generalized gradient approximation (GGA) of the exchange-correlation functional was employed[49], along with the dDsC dispersion correction to account for van der Waals interaction[50]. The cut off energy is 400 eV. The interactions between the atomic cores and electrons were described by the projector augmented wave (PAW) method[51]. All structures were optimized until the force and energy on each atom was less than 0.02 eV/Å and 10^{-6} eV, respectively. A dipole correction in the z direction was used for surface calculations. The transition state search was conducted with the climbing image nudged elastic band (CI-NEB) method, followed by the dimer method to converge the saddle point within 0.05 eV/Å[52].

The calculations of Gibbs free energies include thermal effects, zero-point energies, and entropic contributions, where translational, rotational, and vibrational degrees of freedom were taken into account for gaseous species. For surface species, Harmonic Oscillator (HO) approximation was used and only vibrational contributions were considered. Using this approximation, we can calculate the internal energy (U) and entropy of the adsorbate as follows:

$$U(T) = E_{elec} + E_{ZPE} + \sum_{i}^{harm\ DOF} \frac{\epsilon_i}{e^{\epsilon i/k_B T} - 1}$$

$$S = k_B \sum_{i}^{harm\ DOF} \left[\frac{\epsilon_i}{k_B T(e^{\epsilon i/k_B T} - 1)} - ln(1 - e^{-\epsilon i/k_B T})\right]$$

Where, ϵ_i are the harmonic energies for the adsorbate atoms.

The Helmholtz free energy (F) can hence be calculated as:

$$F(T) = U(T) - TS(T)$$

Assuming that the pV term in $H = U$ + pV is negligible, the Helmholtz Free energy can be used as an approximate for the Gibbs Free energy since $G \approx F$. In total, four-layer (4×4)-

RhRu(111) and four-layer (4*1)-RhRu(211) slabs were used in the calculations. For (211) surface, we sample the most stable configuration for RhRu in the top two layers as a ratio of Rh:Ru as 2:1. The most stable one (**Figure S20**) was chosen for further calculation. For these periodicities, the Brillouin zone was sampled using (5 × 5 × 1), (3 × 5 × 1) Gamma-point-centered K-meshes for (111) and (211) surfaces, respectively. The bottom two layers are fixed while the upper two layers were relaxed during optimization. The formation free energy (G_f) of hydroxylated surface shown in **Figure S21** is calculated as:

$$G_f = G(RhRu(OH)_x) + x\mu(H) - G(RhRu) - xG(H_2O)$$

$$= G(RhRu(OH)_x) + x\,(1/2G(H_2) - eU - ln10\,k_BT\,pH) - G(RhRu) - xG(H_2O)$$

Where *U* is the electrode potential at SHE scale. The pressures of H_2 and H_2O are set as 1atm.

Acknowledgements

X.D. acknowledges support from the National Science Foundation award 1800580. Y.H. acknowledges the gracious support by NewHydrogen, Inc. D.C. and P.S. acknowledge support from the National Science Foundation award 2103116. D. C. and S. K. used the HOFFMAN2 cluster at the UCLA Institute for Digital Research and Education (IDRE)

Conflict of Interest

The authors declare no conflict of interest.

References

[1] J. K. Niemeier, D. P. Kjell, *Organic Process Research & Development* **2013**, *17*, 1580-1590.
[2] T. Sakamoto, A. Serov, T. Masuda, M. Kamakura, K. Yoshimoto, T. Omata, H. Kishi, S. Yamaguchi, A. Hori, Y. Horiuchi, T. Terada, K. Artyushkova, P. Atanassov, H. Tanaka, *J. Power Sources* **2018**, *375*, 291-299.
[3] Who, in *Conference of the IARC Monographs on the Evaluation of Carcinogenic Risks to Humans, Vol. 95*, Lyon, FRANCE, **2006**, pp. 9-38.
[4] B. T. Zhao, J. Song, R. Ran, Z. P. Shao, *Int. J. Hydrogen Energy* **2012**, *37*, 1133-1139.
[5] L. Zhou, X. Luo, L. Xu, C. Wan, M. J. C. Ye, *Catalysts* **2020**, *10*, 930.
[6] H. Liu, Y. Liu, M. Li, X. Liu, J. Luo, *Materials Today Advances* **2020**, *7*.

[7] P. P. Tang, X. Lin, H. Yin, D. X. Zhang, H. Wen, J. J. Wang, P. Wang, *Acs Sustainable Chemistry & Engineering* **2020**, *8*, 16583-16590.
[8] G. Feng, L. An, B. Li, Y. X. Zuo, J. Song, F. H. Ning, N. Jiang, X. P. Cheng, Y. F. Zhang, D. G. Xia, *Nat. Commun.* **2019**, *10*.
[9] Y. Liu, J. H. Zhang, Y. P. Li, Q. Z. Qian, Z. Y. Li, Y. Zhu, G. Q. Zhang, *Nat. Commun.* **2020**, *11*.
[10] Y. P. Li, J. H. Zhang, Y. Liu, Q. Z. Qian, Z. Y. Li, Y. Zhu, G. Q. Zhang, *Sci. Adv.* **2020**, *6*.
[11] F. He, N. N. Xia, Y. Zheng, Y. X. Zhang, H. L. Fan, D. L. Ma, Q. H. Liu, X. Hu, *ACS Appl. Mater. Interfaces* **2021**, *13*, 8488-8496.
[12] D. A. Finkelstein, R. Imbeault, S. Garbarino, L. Roue, D. Guay, *Journal of Physical Chemistry C* **2016**, *120*, 4717-4738.
[13] J. Zhang, Y. X. Wang, C. J. Yang, S. Chen, Z. J. Li, Y. Cheng, H. N. Wang, Y. Xiang, S. F. Lu, S. Y. Wang, *Nano Res.* **2021**.
[14] A. O. Elnabawy, J. A. Herron, S. Karraker, M. Mavrikakis, *J. Catal.* **2021**, *397*, 137-147.
[15] Y. Li, Y. Guo, S. F. Yang, Q. B. Li, S. Chen, B. Y. Lu, H. B. Zou, X. C. Liu, X. L. Tong, H. Q. Yang, *ACS Appl. Mater. Interfaces* **2021**, *13*, 5052-5060.
[16] Z. Q. Ding, K. Wang, Z. Q. Mai, G. Q. He, Z. Liu, Z. H. Tang, *Int. J. Hydrogen Energy* **2019**, *44*, 24680-24689.
[17] S. Park, D. Yoon, S. Bang, J. Kim, H. Baik, H. Yang, K. Lee, *Nanoscale* **2015**, *7*, 15065-15069.
[18] K. Wang, B. L. Huang, W. Y. Zhang, F. Lv, Y. Xing, W. S. Zhang, J. H. Zhou, W. X. Yang, F. X. Lin, P. Zhou, M. Q. Li, P. Gao, S. J. Guo, *J. Mater. Chem. A* **2020**, *8*, 15746-15751.
[19] L. Zhao, X. J. Liu, S. Zhang, J. Zhao, X. L. Xu, Y. Du, X. Sun, N. U. Zhang, Y. Zhang, X. Ren, Q. Wei, *J. Mater. Chem. A* **2021**, *9*, 259-263.
[20] M. Li, Z. Zhao, T. Cheng, A. Fortunelli, C. Chen, R. Yu, Q. Zhang, L. Gu, B. V. Merinov, Z. Lin, E. Zhu, T. Yu, Q. Jia, J. Guo, L. Zhang, W. A. Goddard, Y. Huang, X. Duan, *Science* **2016**, *354*, 1414-1419.
[21] M. Li, K. Duanmu, C. Z. Wan, T. Cheng, L. Zhang, S. Dai, W. Chen, Z. Zhao, P. Li, H. Fei, Y. Zhu, R. Yu, Luo, K. Zang, Z. Lin, M. Ding, J. Huang, H. Sun, J. Guo, X. Pan, W. A. Goddard, P. Sautet, Y. Huang, X. Duan, *Nat. Catalysis* **2019**, *2*, 495-503.
[22] X. Fu, Z. Zhao, C. Wan, Y. Wang, Z. Fan, F. Song, B. Cao, M. Li, W. Xue, Y. Huang, X. Duan, *Nano Res.* **2019**, *12*, 211-215.
[23] X. Huang, Z. Zhao, Y. Chen, C.-Y. Chiu, L. Ruan, Y. Liu, M. Li, X. Duan, Y. Huang, *Nano Lett.* **2014**, *14*, 3887-3894.
[24] Y. Wang, G. Wang, G. Li, B. Huang, J. Pan, Q. Liu, J. Han, L. Xiao, J. Lu, L. Zhuang, *Energy Environ. Sci.* **2015**, *8*, 177-181.
[25] R. Crisafulli, V. V. S. de Barros, F. E. R. de Oliveira, T. D. Rocha, S. Zignani, L. Spadaro, A. Palella, J. A. Dias, J. J. Linares, *Appl. Catal. B-Environ.* **2018**, *236*, 36-44.
[26] Q. Xue, H. Huang, J. Y. Zhu, Y. Zhao, F. M. Li, P. Chen, Y. Chen, *Appl. Catal. B-Environ.* **2020**, *278*, 10.
[27] D. C. de Oliveira, W. O. Silva, M. Chatenet, F. H. B. Lima, *Appl. Catal. B-Environ.* **2017**, *201*, 22-28.
[28] M. G. Hosseini, R. Mahmoodi, M. Abdolmaleki, *New J. Chem.* **2018**, *42*, 12222-12233.
[29] G. J. Wang, S. C. Jing, Y. W. Tan, *Sci. Rep.* **2017**, *7*, 10.

[30] N. Jia, Y. P. Liu, L. Wang, P. Chen, X. B. Chen, Z. W. An, Y. Chen, *ACS Appl. Mater. Interfaces* **2019**, *11*, 35039-35049.
[31] J. J. Yang, L. Xu, W. X. Zhu, M. Xie, F. Liao, T. Cheng, Z. H. Kang, M. W. Shao, *J. Mater. Chem. A* **2022**, *10*, 1891-1898.
[32] Z. Y. Wang, L. Xu, F. Z. Huang, L. B. Qu, J. T. Li, K. A. Owusu, Z. Liu, Z. F. Lin, B. H. Xiang, X. Liu, K. N. Zhao, X. B. Liao, W. Yang, Y. B. Cheng, L. Q. Mai, *Adv. Energy Mater.* **2019**, *9*.
[33] C. Tang, R. Zhang, W. B. Lu, Z. Wang, D. N. Liu, S. Hao, G. Du, A. M. Asiri, X. P. Sun, *Angew. Chem.-Int. Edit.* **2017**, *56*, 842-846.
[34] Q. Q. Sun, L. Y. Wang, Y. Q. Shen, M. Zhou, Y. Ma, Z. L. Wang, C. Zhao, *Acs Sustainable Chemistry & Engineering* **2018**, *6*, 12746-12754.
[35] M. Zhang, Z. Q. Wang, Z. Y. Duan, S. Q. Wang, Y. Xu, X. N. Li, L. Wang, H. J. Wang, *J. Mater. Chem. A* **2021**, *9*, 18323-18328.
[36] A. K. Singh, Q. Xu, *Int. J. Hydrogen Energy* **2014**, *39*, 9128-9134.
[37] J. M. Chen, Q. L. Yao, J. Zhu, X. S. Chen, Z. H. Lu, *Int. J. Hydrogen Energy* **2016**, *41*, 3946-3954.
[38] J. Wang, X. B. Zhang, Z. L. Wang, L. M. Wang, Y. Zhang, *Energy Environ. Sci.* **2012**, *5*, 6885-6888.
[39] H. L. Wang, J. M. Yan, Z. L. Wang, S. I. O, Q. Jiang, *J. Mater. Chem. A* **2013**, *1*, 14957-14962.
[40] B. Q. Xia, T. Liu, W. Luo, G. Z. Cheng, *J. Mater. Chem. A* **2016**, *4*, 5616-5622.
[41] S. N. Oliaee, C. L. Zhang, S. Y. Hwang, H. M. Cheung, Z. M. Peng, *Journal of Physical Chemistry C* **2016**, *120*, 9764-9772.
[42] X. Q. Du, C. Du, P. Cai, W. Luo, G. Z. Cheng, *Chemcatchem* **2016**, *8*, 1410-1416.
[43] N. Firdous, N. K. Janjua, M. H. S. Wattoo, *Int. J. Hydrogen Energy* **2020**, *45*, 21573-21587.
[44] F. Guo, H. T. Zou, Q. L. Yao, B. Huang, Z. H. Lu, *Renew. Energy* **2020**, *155*, 1293-1301.
[45] Y. N. Men, J. Su, X. L. Wang, P. Cai, G. Z. Cheng, W. Luo, *Chin. Chem. Lett.* **2019**, *30*, 634-637.
[46] H. T. Zou, S. L. Zhang, X. L. Hong, Q. L. Yao, Y. Luo, Z. H. Lu, *J. Alloys Compd.* **2020**, *835*.
[47] Y. S. Du, J. Su, W. Luo, G. Z. Cheng, *ACS Appl. Mater. Interfaces* **2015**, *7*, 1031-1034.
[48] Y. P. Qiu, Q. Shi, L. L. Zhou, M. H. Chen, C. Chen, P. P. Tang, G. S. Walker, P. Wang, *ACS Appl. Mater. Interfaces* **2020**, *12*, 18617-18624.
[49] J. P. Perdew, K. Burke, M. Ernzerhof, *Phys Rev Lett* **1996**, *77*, 3865-3868.
[50] S. Gautier, S. N. Steinmann, C. Michel, P. Fleurat-Lessard, P. Sautet, *Phys Chem Chem Phys* **2015**, *17*, 28921-28930.
[51] G. Kresse, D. Joubert, *Physical Review B* **1999**, *59*, 1758-1775.
[52] G. Henkelman, B. P. Uberuaga, H. Jónsson, *The Journal of Chemical Physics* **2000**, *113*, 9901-9904.